NMR imaging of cell phone radiation absorption in brain tissue

David H. Gultekin[a,b,1] and Lothar Moeller[c,1]

[a]Memorial Sloan-Kettering Cancer Center, New York, NY 10065; [b]Weill Cornell Medical College, New York, NY 10065; and [c]Bell Laboratories, Alcatel-Lucent, Holmdel, NJ 07733

A method is described for measuring absorbed electromagnetic energy radiated from cell phone antennae into ex vivo brain tissue. NMR images the 3D thermal dynamics inside ex vivo bovine brain tissue and equivalent gel under exposure to power and irradiation time-varying radio frequency (RF) fields. The absorbed RF energy in brain tissue converts into Joule heat and affects the nuclear magnetic shielding and the Larmor precession. The resultant temperature increase is measured by the resonance frequency shift of hydrogen protons in brain tissue. This proposed application of NMR thermometry offers sufficient spatial and temporal resolution to characterize the hot spots from absorbed cell phone radiation in aqueous media and biological tissues. Specific absorption rate measurements averaged over 1 mg and 10 s in the brain tissue cover the total absorption volume. Reference measurements with fiber optic temperature sensors confirm the accuracy of the NMR thermometry.

nuclear shielding | dipole antenna | mobile communications | SAR | RF safety

Humans are exposed to an increasing amount of nonionizing electromagnetic radiation emitted from sources such as cell phones, power transmission lines, radars, and medical equipment (1), causing public health concerns (2). Safety standards defining upper limits for the specific absorption rates (SARs) were thus established to serve as guidelines for equipment manufacturers in various fields (3–5). Extensive cell phone use is known to present the highest radio frequency (RF) exposure to the general public, prompting this study.

The 6 billion current global cellular phone subscriptions (6, 7) indicate an average airtime of about 30 min/d and an average call length of about 3 min/user (8). Tremendous research efforts starting in the early 1980s to assess the health effects from cell phone radiation have focused on the significant absorption of radiation by those parts of the human brain that are located in close proximity to antennae (9).

In general, the effects of nonionizing radiation have been divided into thermal and nonthermal and have been extensively investigated through cell and animal studies (10–13), neurological studies (14, 15), thermographic measurements (16), computer model–based simulations (17, 18), metabolic human studies (19), and large epidemiological data (20). Among those, researchers have focused on a possible link between cell phone radiation and cancer (21). The International Agency for Research on Cancer (IARC), the cancer research institute of the World Health Organization (WHO), has recently classified RF emission from cell phones as possibly carcinogenic to humans (group 2B) and concluded the aforementioned studies cannot reliably serve to exclude harmful radiation effects, prompting further research (22). This uncertainty can be attributed to limitations of epidemiological data unsuitable for assessing long-term effects and incomplete knowledge of the impact of physical radiation effects on the brain tissue (23–25). Whereas the predominant scientific opinion sees the conversion of absorbed radiation into Joule heat as the dominant effect with possible biological consequences, accurate measurements of its dynamics and magnitude inside the living human body are lacking. Our method intends to fulfill this need by noninvasively and directly measuring the temporal and spatial thermal fields generated by absorbed cell phone radiation in brain tissue.

Current applied methods to characterize SARs compromise measurement accuracy by emulating real cell phone use. Industrial standards for SAR assessment suggest scans of the RF fields with electrical field (E) probes in head phantoms (26), whereas computer-based simulations predict RF field distributions in the head (27). However, such experimental methods are invasive, indirect (E-field probes do not collect temperature data), and lack the required spatial and temporal resolution to measure transient energy deposition rates. 3D measurements with temperature probes require liquid gels in phantoms, and convection caused by probe motion in the gel can disturb the temperature distribution. Moreover, invasive probes perturb the actual radiation and absorption fields at the measurement point, reducing accuracy and leading to measurement errors. Similarly, computer simulations are subject to parameter fitting (electrical conductivity, dielectric constant, thermal conductivity, and specific heat) and often disregard the heterogeneity and perfusion of real tissues. In contrast, NMR imaging allows thermophysical characterization of substances; measurements of thermal diffusivity, thermal conductivity, specific heat, SAR, and the heat transfer coefficients of transient thermal processes (28, 29); perfusion (30); and therapeutically monitoring of hyperthermia and thermal treatment of tumors (31).

Because regular handsets are incompatible with the strong magnetic fields in NMR systems (32), NMR imaging of cell phone radiation absorption requires a unique interdisciplinary approach. Metallic and electronic components can cause projectile hazards, alter magnetic susceptibility of the sample, and eddy currents. They can also interfere with the excitation of nuclei, nuclear magnetization, and relaxation processes. The NMR system itself can also be a significant source of RF power deposition during imaging (33). Through field simulations and empirical studies, we developed an antenna system that meets both safety and SAR measurement standards with minimal to no impact on NMR image acquisition. This NMR-compatible antenna assembly enables noninvasive SAR measurements of cell phone radiation through NMR thermometry, yielding local tissue temperature information in 3D, with high spatial (submillimeter range) and temporal resolution (second range). The temperature affects equilibrium nuclear magnetization, T_1 and T_2 nuclear relaxation times, and NMR frequency. Whereas a number of NMR parameters can be used to measure temperature changes, the frequency shift method is most suitable for imaging large volumes with high spatial and temporal resolutions. The fundamental physical mechanism of frequency

shift is caused by the thermally induced changes in nuclear magnetic shielding. Essentially, heat affects the electrons shielding the nuclei from the external magnetic field and causes a shift in the resonance frequency of nuclei. Because NMR spin phase shift relies on the temperature-dependent nuclear magnetic shielding of hydrogen protons in water (34, 35), which is similar over a wide range of tissue types (36), this method is well suited for thermal imaging of heterogeneous brain tissue.

Cell phone radiation exposure generally depends on emitted RF power, but to some extent this radiation depends on other parameters such as RF frequency, antenna position relative to the head, and the material properties of the absorbing tissue (37). The maximum RF power emitted from handsets available today varies as mobile technology has evolved through generations (1G, 2G, 3G, etc.) using different modulation formats and communication protocols (38–40). Cell phones can emit peak powers of 1–2 W, but through discontinuous transmission, power control, and multiple access techniques such as time division multiplexing (TDMA), their mean output power is much lower. For example, global system mobile (GSM) cell phones at frequencies of 1,800 and 900 MHz with maximum output powers of 1 and 2 W (38) operate at mean powers of 125 and 250 mW, respectively, by enabling eight users to share one channel simultaneously. The RF output power, however, can discretely reach the peak power (1–2 W) in short bursts (0.58 ms) during a call (38). Although, current-generation (3G) cell phones have lower mean output powers (125–250 mW), first-generation (1G) analog phones output significantly higher output powers (600 mW), and future cell phones may generate even more emissions to enable signaling at higher data rates (1). Thus, it is important to investigate a wide range of power levels to include the past, present, and future power emission scenarios as required for epidemiological studies. The Federal Communications Commission (FCC) in the United States has set a SAR limit of 1.6 W/kg averaged over 1 g of tissue for partial-body exposure, whereas the Council of the European Union allows a limit of 2.0 W/kg averaged over 10 g of tissue (41, 42). NMR imaging exceeds these requirements, as mass averaging is limited to a voxel volume (cubic millimeters or milligrams), and time averaging is constrained only by the temporal resolution of the 3D image acquisition (seconds). We defined measurement ranges as even multiples of 6-min irradiation times and 125-mW output powers to study the absorption characteristics of brain tissue. A continuous wave (CW) irradiation (duty factor 1) was applied in our study, but the effects of pulsed irradiation schemes such as TDMA (duty factor 1/8) can also be estimated from these measurements.

Brain tissue has a variable iron concentration that causes magnetic susceptibility heterogeneity-induced contrast in NMR imaging (43). Moreover, such heterogeneity in magnetic and electrical properties of the brain tissue varies with age, causing variations in both NMR imaging and absorption of microwave radiation. Here, we demonstrate the method with an ex vivo bovine brain tissue and a gel phantom, but we will tailor it for in vivo brain tissue measurements in accordance with institutional and regulatory requirements. Our current study only quantifies the thermal effects of the cell phone antenna radiation on animal brain tissue and does not investigate any medical, physiological, or biological effects of cell phone radiation on humans.

Results and Discussion

As expected, the magnitude and size of the thermal field evolution in both the ex vivo brain tissue and the water-triton-salt (WTS) gel were commensurate ($\pm10\%$) because of their similar electrical and thermal parameters, dependent on the radiated power and irradiation time and reproducible as shown in two different measurement series three weeks apart.

Thermal images corresponding to multiple power levels and irradiation times in a 5-mm-thick slice of ex vivo brain tissue in
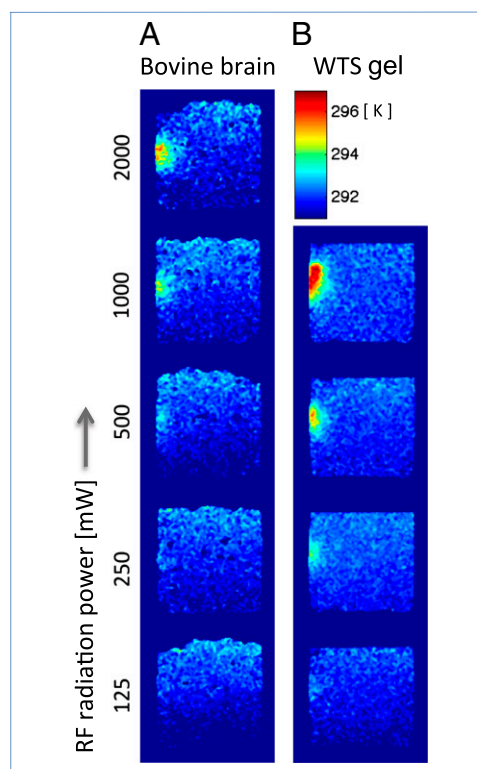

Fig. 1. Thermal images corresponding to power levels of 125, 250, 500, 1000, and 2000 mW and irradiation times of 12 min in a 5-mm slice taken in the center of imaging slab (IP1). (A) Ex vivo bovine brain tissue. (B) WTS gel. Convection becomes apparent in the WTS gel at power levels >1 W after a few minutes of irradiation distending the hot spot shape.

the center of the imaging slab are shown (Fig. 1A) (IP1). Although heating at 125 and 250 mW is hardly visible in the images, a quantitative analysis of the data demonstrates the magnitude of heating at these power levels (Fig. 2).

The corresponding thermal images for the WTS gel are plotted (Fig. 1B). Because of the gel homogeneity, the hot spot appears clear even at the lowest RF radiation power. We exposed the gel to a maximum of 1 W power, beyond which melting ensues and the onset of thermal convection after a few minutes of radiation.

Partial volume effects were apparent between the NMR thermometry and the fiber optic sensor, which samples a volume of about 0.12 mm^3 compared with 2.4 and 1.2 mm^3 for IP1 and IP2, respectively. Note, by averaging over 4 × 4 voxels, such volume ratios can reach 160–320 for IP1 and IP2, respectively. Moreover, unintended bending of the flexible optical fiber while inserting into the phantoms leads to variation of the sensor position even within a single voxel. With first-order approximations, NMR thermometry data analysis averages over temperature gradients inside a voxel, whereas a fiber optic sensor probes the temperature in a comparably small part of it. We compared both quantities that are, in principle, of different thermal nature by introducing a scaling factor (s_f), relating the temperature measurement of the fiber optic sensor (T_f) to that of the NMR (T_N) as $T_f = s_f \cdot T_N$, which ranged from nearly unity (high power) to 0.25 (low power). The relation between the temporal variations of the temperature distribution from two different voxels depends on the distance, power level, specific heat, and thermal diffusivity (29).

Fig. 2 shows transient temperature variations in the ex vivo brain tissue and WTS gel over time along with reference measurements from the fiber optic temperature sensor. The product of specific heat (C) and the temporal derivative of temperature
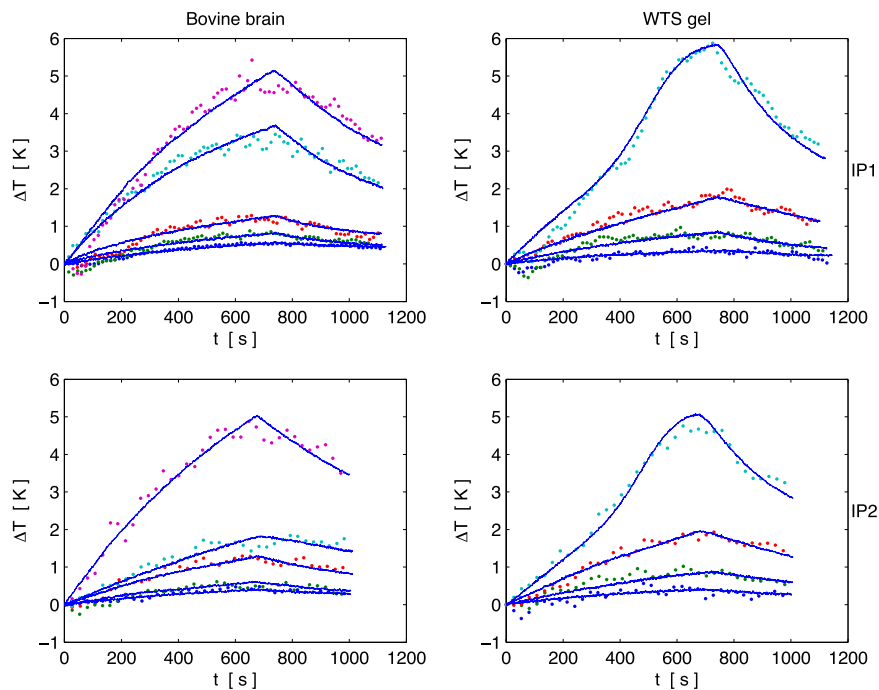
Fig. 2. Temperature evolution in ex vivo bovine brain tissue (left column) and WTS gel (right column) for IP1 (*Upper* row) and IP2 (*Lower* row), respectively. Temperature measurements by NMR (dotted lines) and fiber optic sensor (solid lines) are shown for comparison.

(dT/dt) yields the SAR in ex vivo brain tissue and the gel (in the absence of perfusion and thermal conduction). For in vivo tissue, the local temperature rise can be approximated by Pennes' bioheat equation (44)

$$\frac{\partial T}{\partial t} = \frac{SAR}{C} - \rho m_b \Delta T + \alpha \nabla^2 T, \qquad [1]$$

where $SAR = \sigma|E|^2/\rho$, σ is the electrical conductivity (S/m), ρ is the density (kg/m^3), E is the electric field (V/m), m_b is the volumetric perfusion rate of blood (m^3/kg · s), $\Delta T = T - T_0$, T_0 is the initial temperature (K), and α is the thermal diffusivity (m^2/s). Essentially, all of these terms, temporal and spatial variations of temperature, as well as perfusion, can be measured by NMR imaging in vivo, yielding the SAR distribution (28–30).

The WTS has a slightly higher electrical conductivity but lower permittivity and specific heat, resulting in higher temperature rise per unit power, as indicated by Eq. **1** and observed in our measurements. However, different strong antenna coupling depending on its distance from the container surface can also produce these effects and requires further investigation.

As a proof of concept, NMR thermometry provided 3D images of the thermal fields with the spatial and temporal resolutions suitable for characterization of absorption of RF radiation emitted by cell phone antennas in ex vivo brain tissues. However, the measurements of energy deposition and temperature in ex vivo tissues are free from perfusion effects, and this study essentially presents the worst case scenario in terms of radiation-heated brain tissue. The temperature rise in the in vivo brain tissue is expected to be smaller because of perfusion (45). The method enables SAR measurements averaged over 1 mg and 10 s in the brain tissue covering the entire absorption volume of a human head. However, our experiment shows optimized NMR parameters can be leveraged to visualize even small heating (<1 K) by absorption of cell phone radiation, relevant to in vivo brain tissue SAR measurements. Although the WTS gel emulates electrical and thermal

properties of brain tissue well, it exhibits multiple chemical shifts causing phase resonances and effects on the magnitude of the signal at certain echo times, complicating the NMR thermometry data analysis. Analyzing those effects and the impact of the voxel resolution in relation to partial volume effects is important for further improvement of our method.

In NMR imaging, the acquisition parameters are interdependent and need to be optimized to achieve adequate spatial and temporal resolutions. The volume of the hot spot generated by absorbed cell phone radiation depends on the antenna power level and the irradiation time. This method was optimized to measure a wide range of power levels (125, 250, 500, 1,000 and 2,000 mW) in a larger volume, but it can also be optimized to measure lower power levels (e.g., 31, 62, 125, and 250 mW) in a smaller volume (28, 29). On further refinement of this method, we expect that visualization of the heating of in vivo brain tissues will become feasible and be approved by the Institutional Review Board in accordance with the regulatory requirements for low-power measurements.

Materials and Methods

Aqueous gel composed of 62.7% (wt/vol) water (H$_2$O), 36.8% (wt/vol) octylphenol ethylene oxide condensate [C$_{14}$H$_{22}$O(C$_2$H$_4$O)$_n$ n = 9–10] surfactant (Triton X-100, Union Carbide), and 0.5% sodium chloride (NaCl) (all by weight), referred here as water-triton-salt (WTS) gel, emulates brain tissue with a target permittivity (ε_r') of 44, electrical conductivity (σ) of 1.4 S/m at 1.9 GHz RF frequency (26), and density (ρ) of 1,026 kg/m^3 and possesses semiliquid properties below the temperature of 23 °C. Bovine brain tissue (<2 y of age) readily available for food consumption in some specialty stores was used (within 72 h of extraction) for ex vivo brain experiments. The brain tissue was stored at 277 K (4 °C) and then at 291 K (18 °C) for 24 h in the MRI room to reach thermal equilibrium before our experiments. Both ex vivo brain tissue and the WTS gel possess similar thermal and electrical properties, and equal amounts of them (2,744 cm^3) were filled into PVC containers (14 × 14 × 14 cm^3, 1-mm wall thickness; Fig. 3A), comparable to the volume of an adolescent head (46). Although the thermal properties of substances can be measured by NMR methods (29), standard values were taken from the literature to avoid error accumulation in the data analysis. The specific heat for WTS gel was calculated as 3,730 J/kg · K by extrapolating the data as
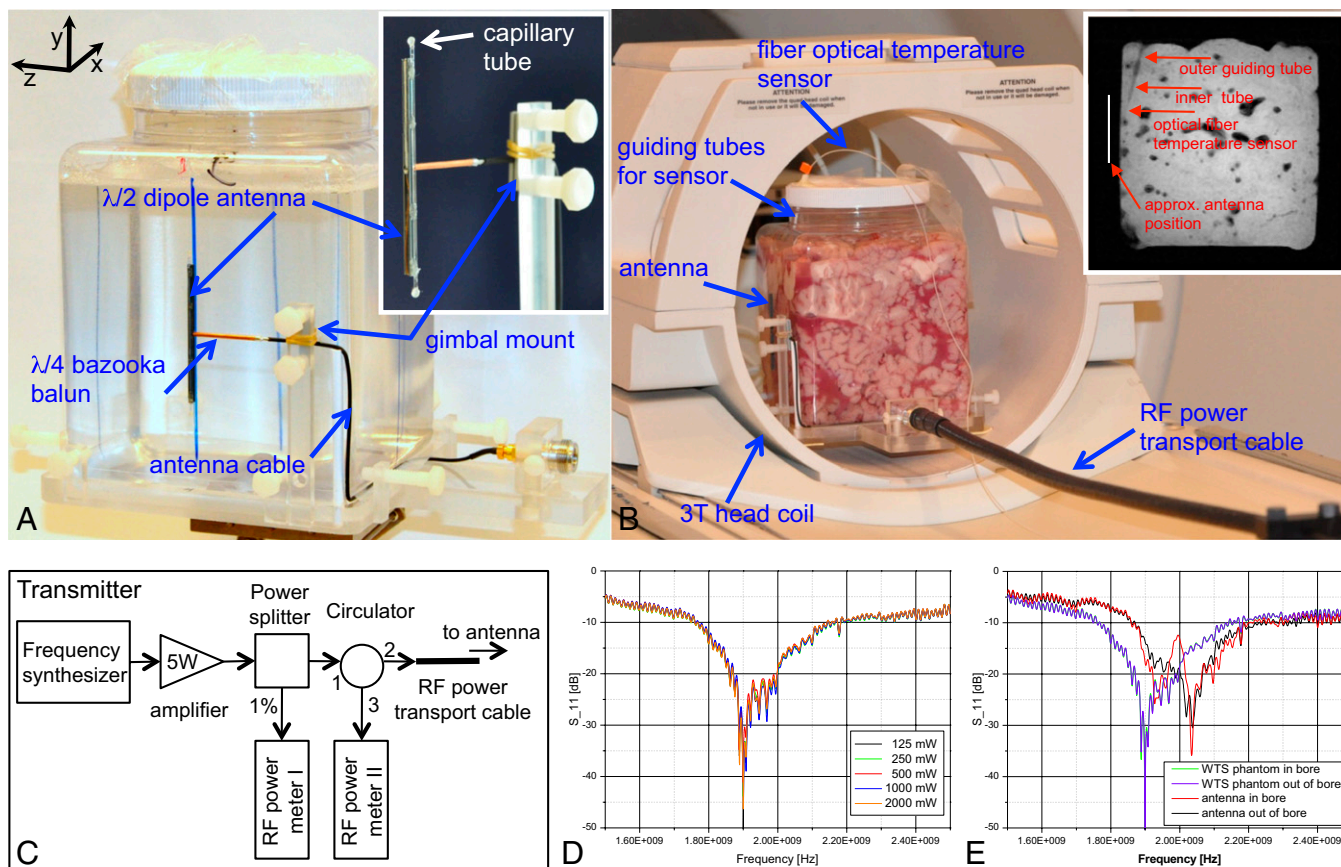
Gultekin and Moeller

Fig. 3. Experimental setup for NMR thermometry of absorbed cell phone radiation. (*A*) WTS gel placed in front of an MRI-compatible λ/2-dipole antenna assembly. (*B*) MRI head coil holding antenna stand loaded with brain tissue and a fiber optic temperature sensor visible in high-resolution magnitude image (*inset*). (*C*) Block diagram of RF transmitter. (*D*) Almost identical S₁₁ resonance curves for five brain tissue measurements confirm reproducible antenna alignment. (*E*) S₁₁ curves taken in and outside the bore show weak impact of MRI environment on loaded antenna.

a function of composition of Triton (47) and taken as 3,826 J/kg · K for a whole brain including average white and gray matter (48). The averages for the real part (ϵ_r') of the dielectric constant and the electrical conductivity (σ) were measured at 1.9 GHz to be 48.1 and 44.4, and 1.30 and 1.41 S/m for the brain tissue and WTS gel, respectively, using a dielectric probe (85070E; Agilent Technologies) with a manufacturer-specified accuracy of about 5%. The measured parameters were location independent inside the WTS gel but varied for the heterogeneous brain tissue from 54.25 to 45.35 and 1.40 to 1.23 S/m for the dielectric constant and electrical conductivity, respectively.

MRI Compatible Cell Phone Antenna. Similar to the IEEE 1528 recommendation but optimized for an MRI environment, a half wavelength (λ/2) dipole antenna made of nonferromagnetic 0.31-mm-diameter coaxial cable and a quarter wavelength (λ/4) copper foil–based bazooka balun (49) was trimmed to an unloaded resonance around 2 GHz. The 0.3-m-long antenna cable (0.5-dB insertion loss at 1.9 GHz; SUCOFORM-47-CU-LSFH; Huber & Suhner) (Fig. 3A) minimally distorts the NMR excitation at 127.4 MHz and the static magnetic fields inside the head coil and is connected to an RF transmitter placed outside the MRI Faraday cage via a 10-m-long nonferromagnetic low-loss RF transport cable (10 mm outer diameter, 1.4 dB insertion loss at 1.9 GHz; S-10162-B-11; Huber & Suhner) (Fig. 3B). The RF transmitter (see block diagram in Fig. 3C) consists of a frequency tunable source, an RF amplifier with 5-W saturation power (SM2023-37LTH; Stealth Microwave), a circulator, and taps to monitor the emitted RF power. A two-axis gimbal mount made

of poly(methyl methacrylate) was used to adjust the tilt and spacing of the dipole arms relative to the container surface. A stand holding the phantom centered the setup inside the head coil (Fig. 3B). With a network analyzer (HP 8753E; Hewlett-Packard) located outside the MRI Faraday cage, we recorded S₁₁ antenna parameters at the input to the RF transport cable. The gimbal mount was tuned until a steep resonance curve was observed. Loading the antenna by moving it closer to the container surface decreases its resonance frequency to ~1.9 GHz as a result of inductive coupling (50). We note hydrostatic pressure inside the PVC container bends its walls, thereby preventing the antenna to orient fully parallel with its surface. At a typical average antenna spacing of about 4 mm relative to the surface, steep S₁₁ dips were obtained (Fig. 3D). Ripples on S₁₁ indicate weak standing waves on the RF transport cable from a small impedance mismatch. Between experiments, the container was rotated 90° to avoid any effects stemming from preheating of one surface from the prior run. Each time, the stand was adjusted to reproduce the S₁₁ curve to find an identical orientation of the antenna relative to the container's surface and achieve a similar radiation condition. A deionized water–filled glass capillary tube (inner diameter, 0.8 mm) was attached parallel to the dipole to visualize the antenna location in MR images relative to the hot spot (Fig. 3A).

The antenna was operated in continuous wave mode (CW) for 12 min (heating phase) at output power levels of 125, 250, 500, 1000, and 2000 mW then turned off for about 6 min (cooling phase). Actual time was recorded electronically.

Table 1. NMR sequence parameters for imaging protocols IP1 and IP2

Imaging Protocol	No. of slices	Slice thickness (mm)	Slab thickness (mm)	Number of phases	Spatial resolution (mm³)	Temporal resolution (s)
IP1	10	5.0	50.0	75	0.7 × 0.7 × 5.0	11.5
IP2	18	2.5	45.0	37	0.7 × 0.7 × 2.5	25.0

PHYSICS

BIOPHYSICS AND COMPUTATIONAL BIOLOGY

MRI Technique. 3D thermal fields of absorbed RF energy were sensed with NMR thermometry using a clinical 3-T NMR imaging scanner (Signa HDx, software version LX14.0; GE Medical Systems) equipped with a birdcage resonator head coil (GEMS, 3T/94) (51). The thermally induced frequency shift is measured by phase shift in imaging as both quantities are related through a time constant called echo time (TE) (52). A nuclear spin phase shift method was adapted and optimized to characterize local temperature variations around the thermal hot spot in the brain tissue and the WTS gel. Two imaging protocols (IP1 and IP2) based on fast gradient echo (GRE) sequences (53) and low NMR-induced SAR provide different spatial and temporal resolutions. The NMR pulse sequences were verified for low SAR through baseline imaging of the entire phantom while the antenna was switched off. Common protocol parameters are as follows: dual echo, bandwidth (BW), 125 kHz; echo times (TE), 2.4 and 5.8 ms; repetition time (TR), 90 ms; imaging matrix, 128 × 256; field of view (FOV), 180 mm × 180 mm. However, IP1 and IP2 differ with respect to the parameters listed in Table 1.

An optical fiber temperature sensor (OTG-MPK5; Opsens) recorded near the hot spot center the temperature evolution in a small volume (0.5 × 0.5 × 0.5 mm^3) inside the phantoms during the NMR imaging to verify the accuracy. The thin optical fiber and gallium arsenide (GaAs) sensor are compatible with the magnetic field in NMR systems and do not contribute magnetic susceptibility and nuclear spin phase shift in the surrounding tissue or gel.

Image Processing for NMR Thermometry. We constructed spin magnitude and spin phase images and unwrapped the phase maps in 2D space using a minimum discontinuity algorithm (54). The spin phase shift was corrected for temporal phase drift by subtracting the phase shift variation from an unheated region in the brain tissue and WTS gel during the same experiment. Spin phase shift maps were then transformed to temperature maps based on the temperature dependence of the nuclear shielding of water (−0.01 ppm/K) in the ex vivo brain tissue and the WTS gel. 3D coordinates of the tip of the fiber optic sensor were located in the high-resolution magnitude

images, and ±2 voxels (volumetric pixel) around these coordinates in the plane of the antenna were averaged in the phase shift images (arithmetically averaging the phase shift measured in radians), yielding sampling volumes of 2.8 × 2.8 × 5 and 2.8 × 2.8 × 2.5 mm^3 for IP1 and IP2, respectively. The temperature measurements by NMR and the fiber optic sensor were plotted on the same time scale for comparison.

The relation between signal to noise ratio (SNR), spatial resolution, and temporal resolution in NMR thermometry needs to be optimized to measure the transient energy deposition in the hot spot. Increasing the spatial and temporal resolution decreases the SNR but increases the temperature measurement uncertainty, especially at low power levels. Increasing voxel sizes enhance the SNR but lead to disagreement between NMR and the optical fiber sensor due to partial volume effects.

Industrial SAR measurement standards recommend a nonmetallic near proximity (<50-cm spacing) of the cell phone under testing to avoid superimposing wave-scattering effects. Here, the MRI RF shield and head coil do not fully comply with this recommendation. Using four different experimental conditions, the head coil loaded with and without WTS phantom and placed inside and outside the MRI bore, we recorded the corresponding S_{11} curves to assess the MRI impact. We did not see differences in the S_{11} curves for the loaded antenna but observed up to first-order approximation, a small negligible variation for the unloaded case, which is expected because the open ends of the RF shield and birdcage coil can form a lossy resonator (Fig. 3E). Our simulations (reported elsewhere), based on a 3D finite-element method (FEM) program (XFdtd; RemCom) mimicking the setup, confirm an insignificant MRI effect on the local SAR values, which may result from cylindrical symmetry and perpendicular dipole orientation.

1. International Commission on Non-Ionizing Radiation Protection (2008) ICNIRP statement on EMF-emitting new technologies. *Health Phys* 94(4):376–392.
2. World Health Organization (2010) *WHO Research Agenda for Radiofrequency Fields* (World Health Organization, Geneva, Switzerland).
3. Osepchuk JM, Petersen RC (2003) Historical review of RF exposure standards and the International Committee on Electromagnetic Safety (ICES). *Bioelectromagnetics* 6(Suppl 6):S7–S16.
4. International Commission on Non-Ionizing Radiation Protection (1998) Guidelines for limiting exposure to time-varying electric, magnetic, and electromagnetic fields (up to 300 GHz). *Health Phys* 74(4):494–522.
5. IEEE (2006) *IEEE Standard for Safety Levels With Respect to Human Exposure to Radio Frequency Electromagnetic Fields, 3 kHz to 300 GHz* [The Institute of Electrical and Electronics Engineers (IEEE), Inc., 3 Park Avenue, New York, NY 10016 USA].
6. International Telecommunication Union (2011) *ICT Facts and Figures* (International Telecommunication Union, Place des Nations, 1211 Geneva 20, Switzerland).
7. United Nations Population Fund (2011) *The State of World Population 2011* (United Nations Population Fund, 605 Third Avenue, New York, NY 10158 USA).
8. CTIA (2011) *Semi-Annual Wireless Industry Survey* (CTIA–The Wireless Association, 1400 16th Street, NW Suite 600, Washington, DC 20036 USA).
9. Adair ER, Petersen RC (2002) Biological effects of radio-frequency/microwave radiation. *IEEE Trans Microw Theory Tech* 50(3):953–962.
10. Lai H, Singh NP (1996) Single- and double-strand DNA breaks in rat brain cells after acute exposure to radiofrequency electromagnetic radiation. *Int J Radiat Biol* 69(4):513–521.
11. Leszczynski D, Joenväärä S, Reivinen J, Kuokka R (2002) Non-thermal activation of the hsp27/p38MAPK stress pathway by mobile phone radiation in human endothelial cells: molecular mechanism for cancer- and blood-brain barrier-related effects. *Differentiation* 70(2–3):120–129.
12. Dewhirst MW, Lora-Michiels M, Viglianti BL, Dewey WC, Repacholi M (2003) Carcinogenic effects of hyperthermia. *Int J Hyperthermia* 19(3):236–251.
13. Blank M, Goodman R (2009) Electromagnetic fields stress living cells. *Pathophysiology* 16(2–3):71–78.
14. Frey AH (1979) Studies of the blood-brain-barrier—Preliminary findings and discussion. *Radio Sci* 14(65):349–350.
15. Salford LG, Brun A, Sturesson K, Eberhardt JL, Persson BR (1994) Permeability of the blood-brain barrier induced by 915 MHz electromagnetic radiation, continuous wave and modulated at 8, 16, 50, and 200 Hz. *Microsc Res Tech* 27(6):535–542.
16. Guy AW, Webb MD, Sorensen CC (1976) Determination of power absorption in man exposed to high-frequency electromagnetic-fields by thermographic measurements on scale models. *IEEE T Bio-Med Eng* 23(5):361–371.
17. Gandhi OP, Kang G (2002) Some present problems and a proposed experimental phantom for SAR compliance testing of cellular telephones at 835 and 1900 MHz. *Phys Med Biol* 47(9):1501–1518.
18. Christ A, Gosselin MC, Christopoulou M, Kühn S, Kuster N (2010) Age-dependent tissue-specific exposure of cell phone users. *Phys Med Biol* 55(7):1767–1783.
19. Volkow ND, et al. (2011) Effects of cell phone radiofrequency signal exposure on brain glucose metabolism. *JAMA* 305(8):808–813.
20. INTERPHONE Study Group (2010) Brain tumour risk in relation to mobile telephone use: results of the INTERPHONE international case-control study. *Int J Epidemiol* 39(3):675–694.
21. US National Research Council (2008) *Committee on Identification of Research Needs Relating to Potential Biological or Adverse Health Effects of Wireless Communications Devices: Identification of Research Needs Relating to Potential Biological or Adverse Health Effects of Wireless Communication Devices* (National Academies Press, Washington, DC).
22. Baan R, et al.; WHO International Agency for Research on Cancer Monograph Working Group (2011) Carcinogenicity of radiofrequency electromagnetic fields. *Lancet Oncol* 12(7):624–626.
23. Ahlbom A, et al.; ICNIRP (International Commission for Non-Ionizing Radiation Protection) Standing Committee on Epidemiology (2009) Epidemiologic evidence on mobile phones and tumor risk: A review. *Epidemiology* 20(5):639–652.
24. Kundi M (2009) The controversy about a possible relationship between mobile phone use and cancer. *Environ Health Perspect* 117(3):316–324.
25. Hardell L, Carlberg M, Hansson Mild K (2011) Re-analysis of risk for glioma in relation to mobile telephone use: Comparison with the results of the Interphone international case-control study. *Int J Epidemiol* 40(4):1126–1128.
26. IEEE (2003) Recommended practice for determining the peak spatial-average specific absorption rate (SAR) in the human head from wireless communications devices: Measurement techniques. *IEEE Std* 1528-2003 (IEEE, Inc., 3 Park Avenue, New York, NY 10016 USA).
27. Cardis E, et al. (2008) Distribution of RF energy emitted by mobile phones in anatomical structures of the brain. *Phys Med Biol* 53(11):2771–2783.
28. Gultekin DH, Gore JC (2010) Measurement of specific heat and specific absorption rate by nuclear magnetic resonance. *Thermochim Acta* 503–504:100–107.
29. Gultekin DH, Gore JC (2011) Simultaneous measurements of thermal conductivity, thermal diffusivity and specific heat by nuclear magnetic resonance imaging. *Thermochim Acta* 519(1–2):96–102.
30. Roberts DA, Detre JA, Bolinger L, Insko EK, Leigh JS, Jr. (1994) Quantitative magnetic resonance imaging of human brain perfusion at 1.5 T using steady-state inversion of arterial water. *Proc Natl Acad Sci USA* 91(1):33–37.
31. Rieke V, Butts Pauly K (2008) MR thermometry. *J Magn Reson Imaging* 27(2):376–390.
32. Schenck JF (1996) The role of magnetic susceptibility in magnetic resonance imaging: MRI magnetic compatibility of the first and second kinds. *Med Phys* 23(6):815–850.
33. Bottomley PA, Andrew ER (1978) RF magnetic field penetration, phase shift and power dissipation in biological tissue: Implications for NMR imaging. *Phys Med Biol* 23(4):630–643.
34. Ramsey NF (1950) Magnetic shielding of nuclei in molecules. *Phys Rev* 78(6):699–703.
35. Hindman JC (1966) Proton Resonance shift of water in gas and liquid states. *J Chem Phys* 44(12):4582–4592.

36. Peters RD, Hinks RS, Henkelman RM (1998) Ex vivo tissue-type independence in proton-resonance frequency shift MR thermometry. *Magn Reson Med* 40(3):454–459.

37. Balzano Q (1999) Exposure metrics for RF epidemiology: Cellular phone handsets. *Radiat Prot Dosimetry* 83(1–2):165–169.

38. Wiart J, Dale C, Bosisio AV, Le Cornec A (2000) Analysis of the influence of the power control and discontinuous transmission on RF exposure with GSM mobile phones. *IEEE T Electromagn C* 42(4):376–385.

39. Vrijheid M, et al. (2009) Determinants of mobile phone output power in a multinational study: Implications for exposure assessment. *Occup Environ Med* 66(10):664–671.

40. Kelsh MA, et al. (2011) Measured radiofrequency exposure during various mobile-phone use scenarios. *J Expo Sci Environ Epidemiol* 21(4):343–354.

41. Federal Communications Commission (2001) *OET Bulletin 65 Supplement C* (Federal Communications Commission, Washington, DC).

42. Council of the European Union (1999) Council recommendation of 12 July 1999 on the limitation of exposure of the general public to electromagnetic fields (0 Hz to 300 GHz). *J Eur Communities* 199:59–70.

43. Fukunaga M, et al. (2010) Layer-specific variation of iron content in cerebral cortex as a source of MRI contrast. *Proc Natl Acad Sci USA* 107(8):3834–3839.

44. Foster KR, Glaser R (2007) Thermal mechanisms of interaction of radiofrequency energy with biological systems with relevance to exposure guidelines. *Health Phys* 92(6):609–620.

45. Burr JG, Krupp JH (1980) Real-time measurement of RFR energy distribution in the Macaca mulatta head. *Bioelectromagnetics* 1(1):21–34.

46. Rollins JD, Collins JS, Holden KR (2010) United States head circumference growth reference charts: Birth to 21 years. *J Pediatr* 156(6):907–913, e1–e2.

47. Jha R, Ahluwalia JC (1994) Test of the additivity rule for the estimation of standard partial molar heat capacities and volumes of some nonionic surfactants in aqueous solutions. *J Phys Chem* 98(37):9115–9118.

48. Bowman HF, Cravalho EG, Woods M (1975) Theory, measurement, and application of thermal properties of biomaterials. *Annu Rev Biophys Bioeng* 4(00):43–80.

49. Sevick J (2003) *Understanding, Building, and Using Baluns and Ununs: Theory and Practical Designs for the Experimenter* (CQ Communications, Hicksville, NY).

50. Kuster N, Balzano Q (1992) Energy-absorption mechanism by biological bodies in the near-field of dipole antennas above 300 MHz. *IEEE T Veh Technol* 41(1):17–23.

51. Hayes CE (2009) The development of the birdcage resonator: A historical perspective. *NMR Biomed* 22(9):908–918.

52. Ishihara Y, et al. (1995) A precise and fast temperature mapping using water proton chemical shift. *Magn Reson Med* 34(6):814–823.

53. Haase A, Frahm J, Matthaei D, Hanicke W, Merboldt KD (1986) Flash imaging—Rapid NMR imaging using low flip-angle pulses. *J Magn Reson* 67(2):258–266.

54. Flynn TJ (1997) Two-dimensional phase unwrapping with minimum weighted discontinuity. *J Opt Soc Am A Opt Image Sci Vis* 14(10):2692–2701.